nature climate change

LETTERS

PUBLISHED ONLINE: 13 APRIL 2015 | DOI: 10.1038/NCLIMATE2605

Decadal modulation of global surface temperature by internal climate variability

Aiguo Dai[1,2*], John C. Fyfe[3], Shang-Ping Xie[4] and Xingang Dai[5]

Despite a steady increase in atmospheric greenhouse gases (GHGs), global-mean surface temperature (*T*) has shown no discernible warming since about 2000, in sharp contrast to model simulations, which on average project strong warming[1-3]. The recent slowdown in observed surface warming has been attributed to decadal cooling in the tropical Pacific[1,4,5], intensifying trade winds[5], changes in El Niño activity[6,7], increasing volcanic activity[8-10] and decreasing solar irradiance[7]. Earlier periods of arrested warming have been observed but received much less attention than the recent period, and their causes are poorly understood. Here we analyse observed and model-simulated global *T* fields to quantify the contributions of internal climate variability (ICV) to decadal changes in global-mean *T* since 1920. We show that the Interdecadal Pacific Oscillation (IPO) has been associated with large *T* anomalies over both ocean and land. Combined with another leading mode of ICV, the IPO explains most of the difference between observed and model-simulated rates of decadal change in global-mean *T* since 1920, and particularly over the so-called 'hiatus' period since about 2000. We conclude that ICV, mainly through the IPO, was largely responsible for the recent slowdown, as well as for earlier slowdowns and accelerations in global-mean *T* since 1920, with preferred spatial patterns different from those associated with GHG-induced warming or aerosol-induced cooling. Recent history suggests that the IPO could reverse course and lead to accelerated global warming in the coming decades.

The Pacific Decadal Oscillation (PDO; refs 11,12), or more generally the IPO (refs 13,14), switched from a warm phase to a cold phase around 1999[15]. This switch has been associated with a cooling trend since the early 1990s over the Equatorial Central and Eastern Pacific (ECEP; 15° S–15° N, 180°–80° W) that has contributed to the recent hiatus in global-mean *T* (refs 4,5). Modelling studies[1,16,17] have also shown that the IPO can modulate the rate of global warming through changes in ocean heat uptake. Given the well-documented extra-tropical response to tropical forcings[18,19], it is not surprising that IPO-associated sea surface temperature (SST) variations in the ECEP have had a large impact on global-mean *T* (ref. 1). The recent cooling of the ECEP has been accompanied by strengthening trade winds[5] and increasing ocean heat uptake[4,16,17,20], typical of a La Niña event[21] but over decadal timescales. Although these studies all point to a major contribution of the ECEP to the recent global warming slowdown, it is unclear how much of the observed SST change in the ECEP is associated with ICV, particularly the IPO, and how much is due to external forcing change, such as stratospheric aerosols[7–10]. Previous analyses[22,23]

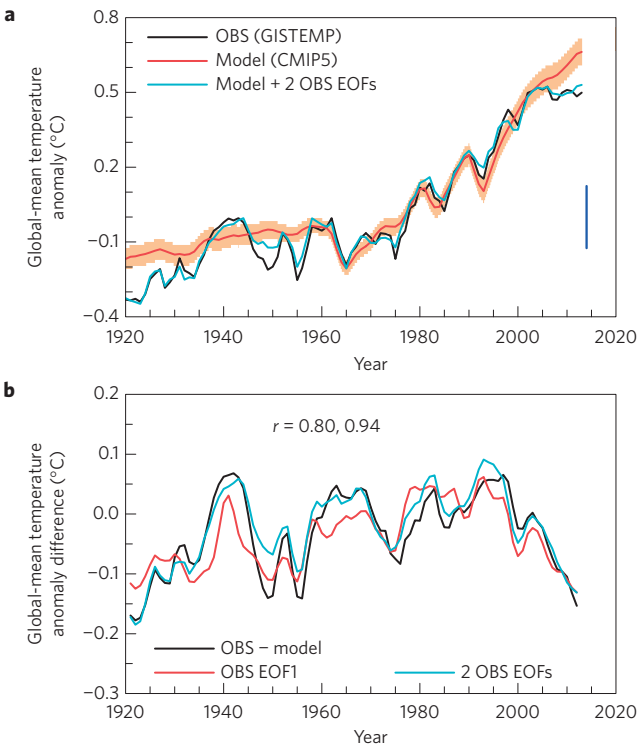

Figure 1 | Time series of the near-global (60° S–75° N) mean surface temperature anomalies (*T*′, all relative to the 1961–1990 mean) from 1920 to 2013. a, Annual *T*′ from the GISTEMP observational data set[26] compared with the ensemble mean surface air temperature from 66 historical all-forcing runs from 33 CMIP5 models multiplied by a scaling factor of 0.863, and the scaled model *T*′ plus the *T*′ represented by the two leading EOFs given in Fig. 2. The contribution of the two leading EOFs is shown as the blue line in **b**. **b**, Three-year moving averaging was applied to the local *T* time series before regional averaging or EOF analyses in this study and also to the lines in **b**. The correlation coefficient (*r*) is for the black versus red and black versus blue lines, respectively. The scaling removes the overall warming bias in the models and improves visual agreement between the observations and models, but does not affect the decadal change patterns (Supplementary Section 4 and Supplementary Fig. 2). The orange shading in **a** represents the 95% confidence interval of the model ensemble mean (red curve) and the blue vertical bar indicates the 10th to 90th percentile range of the internal variability of *T*′ estimated using the CESM1 30-member ensemble simulations[29].

[1]Department of Atmospheric & Environmental Sciences, University at Albany, SUNY, Albany, New York 12222, USA. [2]National Center for Atmospheric Research, PO Box 3000, Boulder, Colorado 80307, USA. [3]Canadian Centre for Climate Modeling and Analysis, Environment Canada, Victoria, British Columbia V8W 2Y2, Canada. [4]Scripps Institution of Oceanography, University of California at San Diego, La Jolla, California 92093, USA. [5]RCE-TEA, Institute of Atmospheric Physics, Chinese Academy of Sciences, Beijing 100029, China. *e-mail: adai@albany.edu

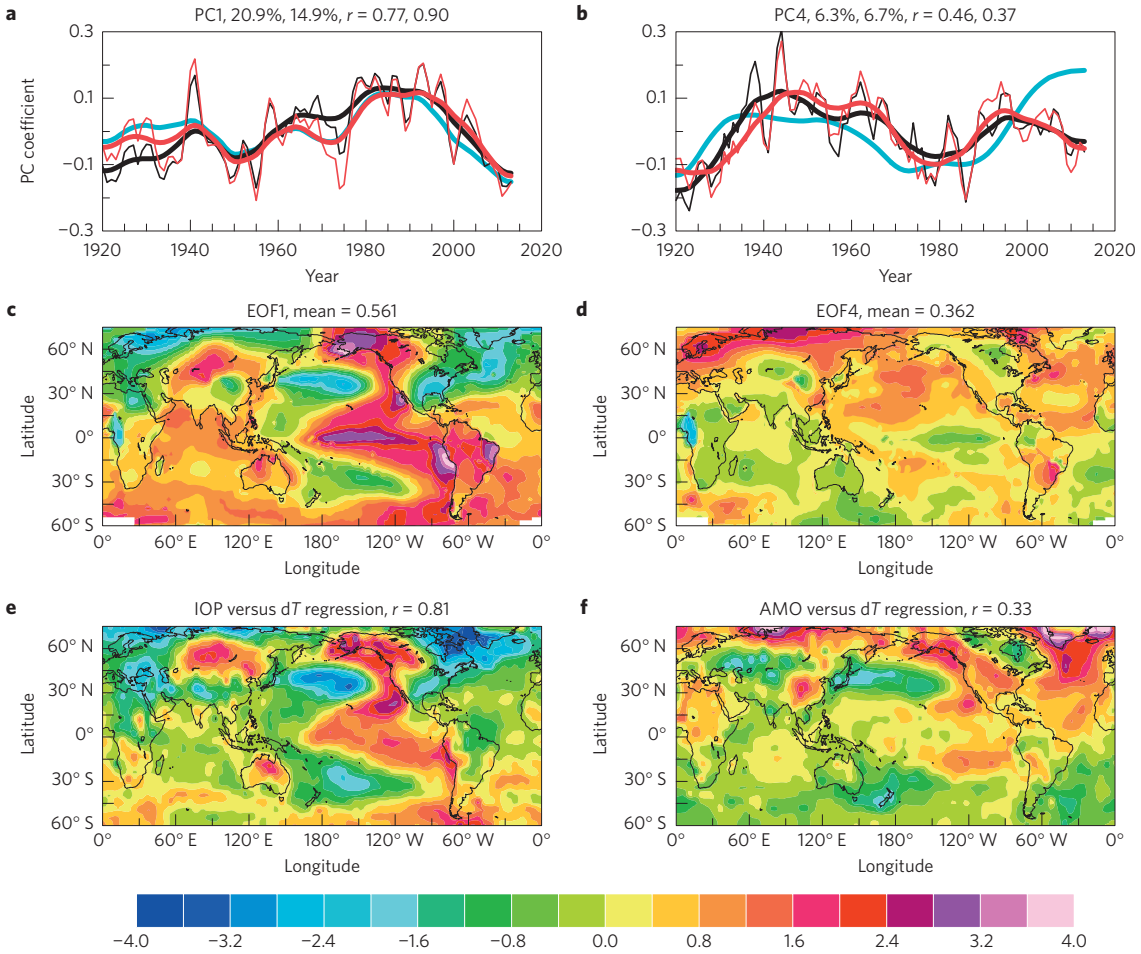

Figure 2 | Time series of the principal components and spatial patterns of the first and fourth leading EOFs in the near-global surface temperature fields during 1920–2013. a,**b**, Time series of the principal components of the first (**a**) and fourth (**b**) EOFs. Thin (thick) lines represent the annual (nine-year smoothed) PCs for the GISTEMP (ref. 26; black) and HadCRUT4 (ref. 27; red) temperature data sets. The blue lines in **a** and **b** indicate the IPO and AMO index, respectively, estimated as the nine-year smoothed PC2 of global SST fields from GISSTEMP and PC1 of the detrended SST over the North Atlantic (20°–70° N, 70° W–0°) domain. Global-mean SST time series from observations was used to detrend the SST data locally through linear regression before estimating the AMO PC. The percentage variance explained by the EOF mode is shown above, from left to right, for GISTEMP and HadCRUT4, respectively. The *r* values shown above are, from left to right, the correlation coefficients between the blue line and thick black line, and the blue line and thick red line, respectively. **c**,**d**, Spatial patterns of the first (**c**) and fourth (**d**) leading EOFs. The EOFs for the HadCRUT4 (not shown) data set are similar to the GISTEMP data set shown here. The area-weighted global mean of the EOF patterns is shown above the plots. **e**, Map of the IPO index (blue line in **a**) versus HadCRUT4 *T* regression slope after detrending using its own global-mean *T* through linear regression. **f**, Map of the AMO index (blue line in **b**) versus HadCRUT4 *T* regression slope after the global trend and IPO components have been removed. The *r* values above **e** and **f** are the area-weighted pattern correlation coefficients between the regression map and the corresponding EOF panels in **c** and **d**, respectively.

suggest that changes in the Atlantic Multidecadal Oscillation (AMO; ref. 24) may have been associated with the rapid global warming since the late 1970s, but these and other[25] studies did not address how the AMO, IPO and other decadal modes of ICV modulated global-mean *T* before the 1970s and during the early twenty-first century. The rate of global warming from 2000 to 2013 also remains to be fully reconciled between observations and climate models. Furthermore, the *T* change patterns (Supplementary Fig. 1) suggest that the recent warming hiatus resulted from a cancellation of warming over most land areas and the Atlantic and Indian Oceans by cooling concentrated over the eastern Pacific Ocean, and that recent natural or anthropogenic aerosol forcing or GHG increases cannot explain the observed *T* change patterns.

Here we quantify the contribution of ICV to the historical evolution of global-mean *T*, including over the warming hiatus period since about 2000. We average over a large number of Coupled Model Intercomparison Project Phase 5 (CMIP5) simulations to derive an estimate of the forced response in global-mean *T* to GHG and other external forcing changes (see Methods). Changes associated with this estimate of the forced response in global-mean *T* are then removed via linear regression from the time series of observed *T* (refs 26,27) at each gridpoint (see Supplementary Information). The goal of the CMIP5-based detrending is to remove forced *T* changes, so that the residual is mostly due to ICV. We choose this over other detrending methods for this purpose as the CMIP5 ensemble mean represents our best estimate of the forced change. Having removed the externally forced component in observed *T*, we then perform an empirical orthogonal function (EOF) analysis (see Supplementary Information) to examine the contributions of the leading modes of ICV to decadal changes in global-mean *T*. We focus on the 1920–2013 period, as observations are sparse in the tropical Pacific and many other regions before 1920. We note that the CMIP5 models on average overestimate the observed warming from 1920 to 2013 by about 14% (see Supplementary Information). As this model bias is not the focus of our study, it is removed

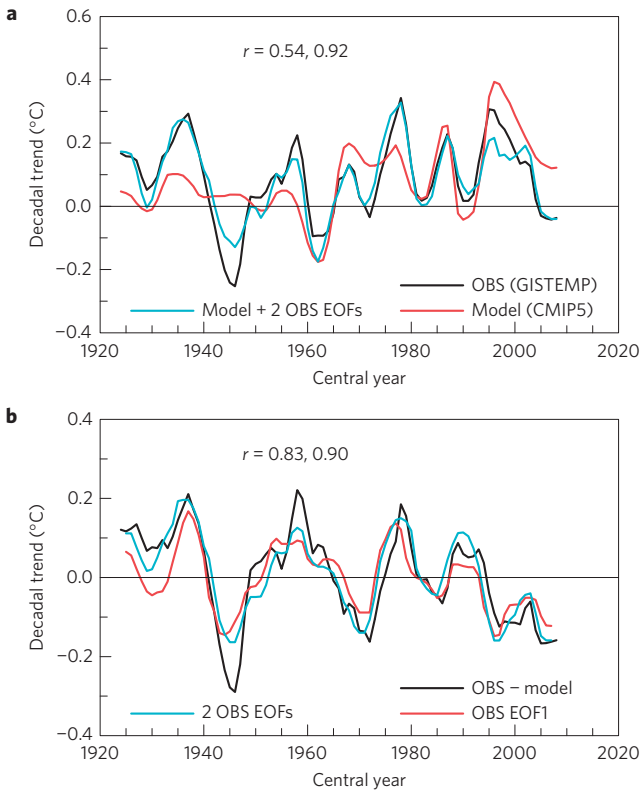

Figure 3 | Evolution of decadal trends in global-mean surface temperatures. a, Rolling ten-year trends corresponding to the curves in Fig. 1a, which have been pre-smoothed using three-year running averages before computing the trend, plotted at the fifth year of the period. **b**, Rolling ten-year trends for the correspondingly coloured lines in Fig. 1b. The black line is the difference between the black and red lines in **a**. In **a** and **b** the correlation coefficients (r) are, from left to right, for the black versus red and black versus blue lines, respectively. The scaling applied to Fig. 1a has little influence on the decadal change rates shown here.

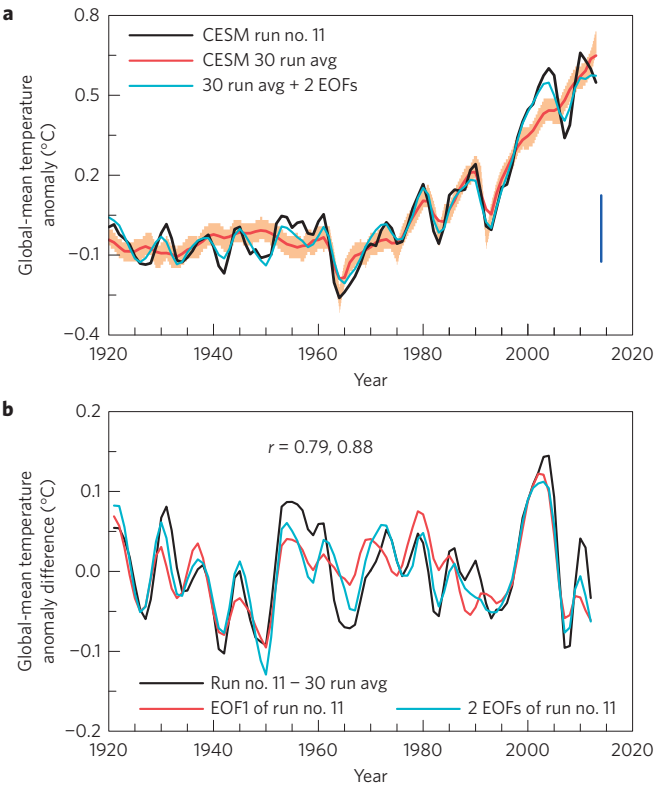

Figure 4 | Simulated time series of the near-global mean surface temperature anomalies (relative to the 1961–1990 mean) from 1920 to 2013 . As Fig. 1 but with the black line for T' taken from CESM1 historical run no. 11 and the red line from the CESM1 30-member ensemble[29] mean T' (without re-scaling). The leading EOF1 and EOF2 of run no. 11 are used in this plot. The orange shading in **a** represents the 95% confidence interval of the model ensemble mean (red curve) and the blue vertical bar indicates the 10th to 90th percentile range of the internal variability of T' estimated using the CESM1 30-member ensemble simulations[29].

through re-scaling without affecting our overall conclusions (see Supplementary Section 4).

We find that the first and fourth leading EOFs of the ICV can account for the large decadal swings in observed global-mean T, for example, by up to ±0.1 °C around 1925, 1940, 1950, and after 2005 (Fig. 1). These fluctuations in observed global-mean T are absent in the corresponding model-mean time series (Fig. 1a), which approximates the mean forced response to historical GHG and other external forcing changes. By construction, the EOF method maximizes the spatially integrated variance explained by the leading EOFs, but it does not require them to explain any variations in the global-mean T. In fact, EOFs 2 and 3 contribute little to the global-mean T, as their spatial patterns approximately cancel each other. Thus, it is surprising that it takes only two EOF modes to explain most (88%) of the observed global-mean T deviations from the forced response. The re-scaling of the model T in Fig. 1 improves the visual agreement with the observations, but even without this re-scaling the two EOFs still account for most (67%) of the observed decadal T variations (Supplementary Fig. 2).

The first EOF mode (Fig. 2a,c) resembles (but is not identical to) the temporal and spatial patterns of the previously defined PDO (refs 11,12), or the IPO (refs 13–15), as its PC series is highly correlated ($r = 0.77$ and 0.90 for the GISTEMP and HadCRUT4 cases, respectively) with the IPO index (blue line in Fig. 2a). Spatial patterns of EOF1 over the oceans also resemble the SST patterns associated with the PDO (refs 11,12) or IPO (ref. 15). The patterns of the detrended T regression against the IPO index (Fig. 2e) are also highly correlated ($r = 0.81$) with the patterns of EOF1 (Fig. 2c). The EOF1 patterns over many land areas (for example, around the Pacific rim) are spatially coherent with the SST patterns over the oceans (Fig. 2c). Thus, we conclude that EOF1 represents the impact of the IPO, a prominent physical mode of ICV (ref. 24), on surface T. The fourth EOF (Fig. 2b,d), with large loading in the Northern Hemisphere including the North Atlantic, partially resembles the temporal and spatial structures of the AMO, as well as the surface temperature patterns associated with the West Pacific Oscillation[28]. Its temporal and spatial structures do not resemble any known historical external forcing, but its underlying physical nature requires further investigation.

These leading EOF modes are similar between the GISTEMP and HadCRUT4 data sets, although small differences exist, mainly in the early part of the record (Fig. 2a–d). The IPO mode accounts for more variance in the GISTEMP data set than in the HadCRUT4 data set (that is, 20.9% and 14.9%). Together, EOF modes 1 and 4 of ICV identified here explain only about 27.2% (21.6%) of the total spatially integrated variance in the detrended annual-mean temperature from the GISTEMP (HadCRUT4) data set, yet they account for essentially all the decadal variations in global-mean T. As there is little evidence that the IPO and the other decadal mode of ICV have been significantly influenced by anthropogenic forcing so far[3], we reasonably assume them to primarily represent unforced internal climate variations. On the basis of Figs 1 and 2, we conclude that the decadal differences between the observed and model-simulated global-mean T anomalies since 1920 are largely

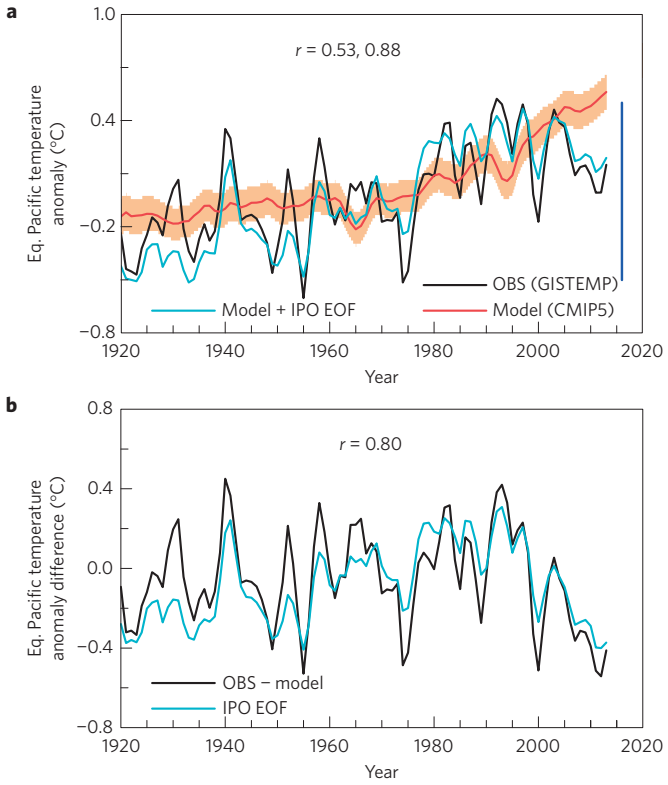

Figure 5 | Time series of the ECEP surface temperature anomalies (T', all relative to the 1961–1990 mean) from 1920–2013. a, Annual T' from the GISTEMP observational data set[26] (black) compared with the ensemble mean surface air temperature from 66 historical all-forcing runs from 33 CMIP5 models multiplied by a scaling factor of 0.863 (red), and the scaled model T' plus the T' represented by the first leading EOF (blue). **b**, GISTEMP minus the scaled model T' difference (black) and the ECEP T' represented by the first leading EOF (blue). The correlation coefficient (r) is, from left to right, for black versus red and black versus blue lines in **a** and between the two lines in **b**. The orange shading in **a** represents the 95% confidence interval of the model ensemble mean (red curve) and the blue vertical bar indicates the 10th to 90th percentile range of the internal variability of T' estimated using the CESM1 30-member ensemble simulations[29].

accounted for by the IPO and the other leading mode of ICV identified here.

The observed rate of change in global-mean T over individual ten-year periods has varied widely, ranging from warming of about 0.3 °C per decade during the late 1930s and late 1970s to cooling of similar magnitude in the 1940s (Fig. 3a). The corresponding rates of change derived from the two leading modes of ICV (that is, EOF1 and EOF4) account for most (81%) of the observation-minus-model difference, with the IPO mode explaining most (69%) of it (Fig. 3b). Large differences between the observed and model-mean rates of change similar to those over the 2000–2013 period have occurred in the past—for example, during the 1930s, 1940s and late 1950s. After accounting for the combined contribution from these two leading EOFs, we see that the observed and simulated rates of change match well over the recent period from 2000 to 2013 (Fig. 3a, black and blue curves), although some differences remain during the ten-year period centred around 2002, and during earlier periods in the 1970s and around 1990, for example. Possible causes for these residual differences may include decadal variations in stratospheric aerosols being misrepresented in the CMIP5 simulations[8], as well as deficiencies in simulating the cooling effects of anthropogenic tropospheric aerosols[3]. However, the T change patterns induced by volcanic or anthropogenic aerosols are inconsistent with the recent observations (Supplementary Fig. 1).

We repeated our analysis using the CESM1 30-member ensemble of simulations[29] (Fig. 4). Global-mean T in its run no. 11 happens to change little from 2000 to 2013, in contrast to the steady warming in the 30-member ensemble mean. As a result, there are substantial differences of ~0.1 °C in global-mean T, comparable to those of Fig. 1, between this run and the ensemble mean on multi-year to decadal timescales. As in our observational analysis, these differences can be largely accounted for by the two leading EOFs from run no. 11 (Fig. 4). Further, the spatial patterns of these two EOFs resemble those of the leading EOFs in a free control run by the same model, with both leading EOFs showing IPO-like patterns (Supplementary Fig. 3). These results support our observational analysis that natural variability, specifically IPO, explains most of the inter-decadal variations in global-mean T.

Spatial maps of observed T obtained after removing our estimate of the externally forced component exhibit complex spatial patterns that vary from period to period (Supplementary Fig. 4). These patterns show a close resemblance to the IPO pattern (Fig. 2b) for the hiatus period from 2000 to 2013 (Supplementary Fig. 4g, spatial correlation $r = -0.86$), as well as for the accelerated warming period from 1992 to 1998 (Supplementary Fig. 4c, where $r = 0.76$). These results show that there are preferred spatial patterns associated with the slowdowns and accelerations of global-mean T, with cooling in the central and eastern Pacific Ocean and adjacent land areas during hiatus periods. These patterns differ from those of GHG-induced warming[3] or aerosol-induced cooling (Supplementary Fig. 1).

In the ECEP region from 1920 to 2003, the observed SSTs show an overall upward trend that is comparable to the re-scaled CMIP5 multi-model-mean trend (Fig. 5a). However, since about 2003 the observed SSTs in the ECEP region have decreased whereas the CMIP5 model-mean SSTs continue to rise. Decadal pauses or declines in the long-term rise of observed SSTs in the ECEP region have occurred in the past—for example, from 1940 to 1949 and from 1968 to 1975 (Fig. 5a). However, the departures from the model-mean trends during these periods are not as obvious as during 2000–2013, mainly because the recent period is associated with rapid warming in the models. The observed and simulated T differences in the ECEP region can be largely accounted for by the IPO mode, especially since the late 1970s (Fig. 5b). From 1993 to 2013, the IPO index evolved from a maximum around 1993 to a minimum around 2012, which induced a cooling of about 1 °C in the ECEP region.

We conclude that after accounting for the combined impacts of the IPO and another decadal mode of ICV and for a systematic model bias in global warming magnitude, the observed and model-simulated decadal anomalies of global-mean temperature are consistent with each other since the early twentieth century. In particular, the recent warming hiatus from 2000 to 2013 in observations can be primarily attributed to an IPO transition from a positive to a negative phase. Although it is difficult to predict the future evolution of the IPO (ref. 24), the recent history suggests that the IPO-induced cooling trend may have run its course and reverse soon. Should this happen, we will see accelerated global warming rates within the next few decades.

Methods

Methods and any associated references are available in the online version of the paper.

Received 8 May 2014; accepted 21 February 2015; published online 13 April 2015

References

1. Kosaka, Y. & Xie, S-P. Recent global-warming hiatus tied to equatorial Pacific surface cooling. *Nature* **501,** 403–407 (2013).

2. Fyfe, J. C., Gillett, N. P. & Zwiers, F. W. Overestimated global warming over the past 20 years. *Nature Clim. Change* **3,** 767–769 (2013).
3. IPCC *Climate Change 2013: The Physical Science Basis* (eds Stocker, T. E. *et al.*) (Cambridge Univ. Press, 2013).
4. Trenberth, K. E. & Fasullo, J. An apparent hiatus in global warming? *Earth's Future* **1,** 19–32 (2013).
5. England, M. *et al.* Recent intensification of wind-driven circulation in the Pacific and the ongoing warming hiatus. *Nature Clim. Change* **4,** 222–227 (2014).
6. Kaufmann, R. K., Kauppi, H., Mann, M. L. & Stock, J. H. Reconciling anthropogenic climate change with observed temperature 1998–2008. *Proc. Natl Acad. Sci. USA* **108,** 11790–11793 (2011).
7. Schmidt, G. A., Shindell, D. T. & Tsigaridis, K. Reconciling warming trends. *Nature Geosci.* **7,** 158–160 (2014).
8. Solomon, S. *et al.* The persistently variable "background" stratospheric aerosol layer and global climate change. *Science* **333,** 866–870 (2011).
9. Fyfe, J. C., von Salzen, K., Cole, J. N. S., Gillett, N. P. & Vernier, J-P. Surface response to stratospheric aerosol changes in a coupled atmosphere–ocean model. *Geophys. Res. Lett.* **40,** 584–588 (2013).
10. Santer, B. *et al.* Volcanic contribution to decadal changes in tropospheric temperature. *Nature Geosci.* **7,** 185–189 (2014).
11. Zhang, Y., Wallace, J. M. & Battisti, D. S. ENSO-like interdecadal variability: 1900–93. *J. Clim.* **10,** 1004–1020 (1997).
12. Mantua, N. J., Hare, S. R., Zhang, Y., Wallace, J. M. & Francis, R. C. A Pacific interdecadal climate oscillation with impacts on salmon production. *Bull. Am. Meteorol. Soc.* **78,** 1069–1079 (1997).
13. Power, S, T., Casey, C., Folland, A., Colman, A & Mehta, V. Interdecadal modulation of the impact of ENSO on Australia. *Clim. Dynam.* **15,** 319–324 (1999).
14. Deser, C, Phillips, A. S. & Hurrell, J. W. Pacific interdecadal climate variability: Linkages between the tropics and the North Pacific during boreal winter since 1900. *J. Clim.* **17,** 3109–3124 (2004).
15. Dai, A. The influence of the Inter-decadal Pacific Oscillation on US precipitation during 1923–2010. *Clim. Dynam.* **41,** 633–646 (2013).
16. Meehl, G. A., Arblaster, J. M., Fasullo, J. T., Hu, A. & Trenberth, K. E. Model-based evidence of deep-ocean heat uptake during surface-temperature hiatus periods. *Nature Clim. Change* **1,** 360–364 (2011).
17. Meehl, G. A., Hu, A., Arblaster, J., Fasullo, J. T. & Trenberth, K. E. Externally forced and internally generated decadal climate variability in the Pacific. *J. Clim.* **26,** 7298–7310 (2013).
18. Seager, R., Harnik, N., Kushnir, Y., Robinson, W. & Miller, J. Mechanisms of hemispherically symmetric climate variability. *J. Clim.* **16,** 2960–2978 (2003).
19. Trenberth, K. E., Caron, J. M., Stepaniak, D. P. & Worley, S. Evolution of El Niño–Southern Oscillation and global atmospheric surface temperatures. *J. Geophys. Res.* **107,** 4065 (2002).
20. Balmaseda, M. A., Trenberth, K. E. & Källén, E. Distinctive climate signals in reanalysis of global ocean heat content. *Geophys. Res. Lett.* **40,** 1754–1759 (2013).
21. Neelin, J. D. *Climate Change and Climate Modeling* (Cambridge Univ. Press, 2011).
22. DelSole, T., Tippett, M. K. & Shukla, J. A significant component of unforced multidecadal variability in twentieth century global warming. *J. Clim.* **24,** 909–926 (2011).
23. Wu, Z., Huang, N. E., Wallace, J. M., Smoliak, B. V. & Chen, X. On the time-varying trend in global-mean surface temperature. *Clim. Dynam.* **37,** 759–773 (2011).
24. Liu, Z. Y. Dynamics of interdecadal climate variability: A historical perspective. *J. Clim.* **25,** 1963–1995 (2012).
25. Chen, J., Del Genio, A. D., Carlson, B. E. & Bosilovich, M. G. The spatiotemporal structure of twentieth-century climate variations in observations and reanalyses. Part II: Pacific pan-decadal variability. *J. Clim.* **21,** 2634–2650 (2008).
26. Hansen, J., Ruedy, R., Sato, M. & Lo, K. Global surface temperature change. *Rev. Geophys.* **48,** RG4004 (2010).
27. Morice, C. P., Kennedy, J. J., Rayner, N. A. & Jones, P. D. Quantifying uncertainties in global and regional temperature change using an ensemble of observational estimates: The HadCRUT4 dataset. *J. Geophys. Res.* **117,** D08101 (2012).
28. Barnston, A. G. & Livezey, R. E. Classification, seasonality and persistence of low-frequency atmospheric circulation patterns. *Mon. Wealth. Rev.* **115,** 1083–1126 (1987).
29. Kay, J. E. *et al.* The Community Earth System Model (CESM) large ensemble project: A community resource for studying climate change in the presence of internal climate variability. *Bull. Am. Meteorol. Soc.* http://dx.doi.org/10.1175/BAMS-D-13-00255.1 (2014).

Acknowledgements

We thank K. Trenberth, B. Merryfield and G. Boer for constructive comments, P. Kushner for sharing the CCSM4 ensemble simulations used in Supplementary Fig. 10, and H. Wang for providing the data used in Supplementary Fig. 1b. We acknowledge the CMIP5 modeling groups and NCAR CESM large ensemble project, the Program for Climate Model Diagnosis and Intercomparison and the WCRP's Working Group on Coupled Modelling for their roles in making available the WCRP CMIP multi-model data sets. Support for this data set is provided by the Office of Science, US Department of Energy. A.D. is supported by the National Science Foundation (AGS-1353740) and the US Department of Energy's Office of Science (DE-SC0012602); S-P.X. is supported by the NSF (AGS- 1305719).

Author contributions

A.D. designed the study, performed all the calculations, made most of the figures, and wrote the draft of the paper; J.C.F. helped improve the manuscript and made Supplementary Fig. 10; S-P.X. helped improve the manuscript; X.D. helped initiate the study.

Additional information

Supplementary information is available in the online version of the paper. Reprints and permissions information is available online at www.nature.com/reprints. Correspondence and requests for materials should be addressed to A.D.

Competing financial interests

The authors declare no competing financial interests.

Methods

We used the GISTEMP (ref. 26) and HadCRUT4 (ref. 27) gridded monthly surface T data sets, which incorporate SST observations over oceans and surface air T observations over land. Small data gaps in the HadCRUT4 data set were filled using spatial bilinear interpolation. Model data of monthly surface air T were obtained from 66 historical (1919 to 2005) and RCP4.5 (2006 to 2013) simulations from 33 CMIP5 models[30] (http://cmip-pcmdi.llnl.gov/cmip5/index.html). Model-mean averages were obtained by averaging equally over the 66 available realizations. All observed and simulated fields were interpolated onto a common 2.5° (longitude) by 2.5 ° (latitude) grid. Area-weighted EOF analyses were performed. To focus on decadal- and longer-timescale variations, three-year moving averages were applied to the T anomaly data. All anomalies are relative to the 1961–1990 mean.

To derive an estimate of internally generated variability in observations, we first computed the global-mean T time series from the CMIP5 ensemble mean, and then removed the changes and variations associated with this model T series using linear regression from the observed T time series at each gridpoint. As the model-mean T series contains a primarily forced response, this procedure removes as much as possible the externally forced component from the observations. Similar procedures have been widely used in climate detection and attribution studies[6,31]. After removing the forced component, the observational T fields were subjected to an EOF analysis. Further technical details and validations of this procedure are provided in the Supplementary Information. Ten-year running linear trends were estimated using the pair-wise slope method[32], which was found to outperform conventional least squares fitting for small samples ($N < 40$) in our tests.

The results are similar when the HadCRU4 data set is used as the observations (Supplementary Figs 5–8), although some quantitative differences exist between the GISTEMP and HadCRU4 cases. However, these differences do not change our main conclusions.

To verify our method and examine whether similar conclusions can be made in a coupled climate model, we repeated our analysis using the 30-member ensemble of historical all-forcing runs from the NCAR CESM (ref. 28; http://www.cesm.ucar.edu/experiments/cesm1.1/LE/). We used run no. 11 as the target realization ('observations'), as it had little warming during 2000–2013, and the 30-member ensemble mean as the forced signal (without re-scaling).

References

30. Taylor, K. E., Stouffer, R. J. & Meehl, G. A. An overview of CMIP5 and the experiment design. *Bull. Am. Meteorol. Soc.* **93,** 485–498 (2012).
31. Santer, B. *et al.* Identifying human influences on atmospheric temperature. *Proc. Natl Acad. Sci. USA* **110,** 26–33 (2013).
32. Lanzante, J. R. Resistant, robust and non-parametric techniques for the analysis of climate data: Theory and examples, including applications to historical radiosonde station data. *Int. J. Climatol.* **16,** 1197–1226 (1996).